C.6 Manuscript in Preparation

A copy of the manuscript (Perry et al. *in prep.*) referred to in Chapter 6 is provided for information as it will not be published at the time this thesis is examined. This manuscript details the physics of interferometer, including how the system resolution and limitations are estimated. Note that although the details are similar, the device described below is different from the one presented in Chapter 6. The instrument describer here is the that was initially used when the study in Chapter 2 was completed. An new permanent device for the Paterson apparatus has since been built, made possible by funding from a ANU Major Equipment Grant. We describe this device in Chapter 6.

For the article below KSH, DAS, BJJS conceived the idea. PWFF, LER, BJJS built the instrument, KSH, PWFF, BJJS installed and tested the instrument on the Paterson apparatus, KSH ran the experiments and collected the data, PWFF and BJJS analysed the sensor response. PWFF and KSH wrote the paper and all authors contributed to its review.

Optical Heterodyne Measurement Of High Velocity Single Axis Slip Events

PERRY W. F. FORSYTH[1,*], KATHRYN S. HAYWARD[2], LYLE E. ROBERTS[1], STEPHEN F. COX[2], DANIEL A. SHADDOCK[1], AND BRAM J. J. SLAGMOLEN[1]

[1] OzGrav-ANU, Centre for Gravitational Astrophysics, College of Science, The Australian National University, Acton, ACT 2601, Australia
[2] Research School of Earth Sciences, The Australian National University, Canberra, 2601, Australia
[*] Corresponding author: perry.forsyth@anu.edu.au

Compiled April 16, 2021

We present an architecture for an free-space optical displacement sensor. This sensor utilizes a fiberized Mach-Zehnder based optical heterodyne system coupled with a digital phase lock loop, providing a large dynamic range (multiple centimeters), high displacement resolution ($< 10^{-10}$ m/$\sqrt{\text{Hz}}$ for frequencies above 100 Hz) and high velocity tracking capabilities (up to 12.24 m/s). The displacement sensor was developed to increase the displacement and time sensitivity for measuring laboratory-scale earthquakes induced in geological samples using a triaxial compression apparatus. In this study we present the results of 13 high-velocity slip events occurring on synthetic fault planes in three Fontainebleau sandstone samples.

OCIS codes: (120.4640) Optical instruments;(060.2840) Heterodyne; (120.5060) Phase modulation; (280.4788) Optical sensing and sensors.

http://dx.doi.org/10.1364/ao.XX.XXXXXX

1. INTRODUCTION

Most earthquakes that occur in the Earth's continental crust nucleate at depths of 5-15 km [1, 2]. Presently there is no way of directly observing the nucleation and rupture of natural faults. Consequently, our understanding of the processes that occur during the first crucial moments of slip come from experiments performed in the laboratory using different types of deformation apparatus [3–5]. The apparatus best able to replicate the pressure and temperature conditions at earthquake-producing depths is the triaxial deformation apparatus. This type of apparatus uses a confining medium to apply a uniform pressure to the sample, simulating pressures at depths of 5-15km. Increasing differential stress (difference between maximum and minimum stresses) brings the sample to failure and is applied using hydraulic loading system.

In this study we use a Paterson-type triaxial deformation apparatus [6]. A key feature of this apparatus is its mechanical sensitivity due to the use of a gas confining medium and internal load cell, allowing samples to be deformed at confining pressures up to 300 MPa and differential stresses up to 1 GPa. The study of earthquake slip was not the original intent of the apparatus. Yet the ability of the apparatus to store elastic strain energy in its loading frame that is released into the sample during a slip event, makes it valuable for use in the study of small seismic events. We use pre-ground surfaces on geological materials to simulate a small part of a natural fault.

Traditional mechanical measurements on this type of apparatus have involved the use of sensors such as pressure and displacement transducers, and strain gauges. These types of sensor produce a voltage output sampled at a rate of 1-100 samples per second. Fundamental limitations in sensor response time, signal conditioning requirements and electromagnetic interference from amplifiers and the internal resistance furnace prevent data acquisition rates being increased to levels sufficient to capture seismic slip events.

As a result, measuring displacement under the dynamic conditions associated with fault slip remains poorly constrained due to the difficulty of measuring displacement in a sample contained within the pressure vessel. Two groups have attempted to measure dynamic slip velocity/displacement, both using optical setups [7, 8]. Hayward et al. (2016) presented the first results from the free-space optical displacement sensor presented in this paper, while Lockner et al., (2017) utilized a commercially built laser doppler vibrometer. Since Hayward et al. (2016), there has been continued interest in the development and expansion of the free-space optical displacement sensor system. This has resulted in a need to further document the architecture of the system and detail the current implementation.

Fundamental to the development of a sensor that could accurately measure displacement and velocity during slip were five essential design criteria. These were as follows:

1. The system capable of recording displacement at a temporal

resolution sufficient to capture rupture propagation velocity (estimated as the shear wave velocity of the material [2]) and equates to a sampling rate of 170 kS/s (for the material used in this study).

2. The system must be immune to electromagnetic interference at the measurement point.

3. The system must be able to measure displacements at resolutions <1 μm, track displacement over a large dynamic range (in the order of centimeters) with a dynamic slip velocity in the order of meters per second.

4. The system must allow flexibility of configuration, but not impede the mechanical operation of the apparatus.

5. The system must be able to operate remotely to meet the safety requirements of operating in a hazardous high pressure lab environment.

In the following sections we outline the basic experimental set-up and describe the architecture for our optical sensor. We then provide results that validate the accuracy of the system and confirm that we have meet the design criteria listed above.

2. METHOD

A. Deformation Experiments

A series of deformation experiments designed to simulate micro-slip on faults at seismogenic depths in the Earth's crust were undertaken using a natural pure quartz sandstone (Fontainebleau sandstone, grain size = 180-250 μm; porosity = 6-7 %). Cores of sandstone (diameter = 9.98 mm) were ground at 45° to the cylinder axis and were used to simulate fault interfaces. Two sample segments, representing the different sides of the fault, were ground to an overall length of 21 mm. The assembly, consisting of the sample and ceramic pistons were loaded into a thin walled (0.4 mm) annealed copper jacket which was used to maintain alignment of the different components during the experiment and separate the Argon confining medium from the sample assembly.

Experiments were undertaken using a Paterson gas-medium, rock deformation apparatus (Fig. 1). The sample assembly was connected to the loading frame via a series of steel pistons at the top and bottom of the assembly. An axial load was applied to the specimen via the pistons by lowering the upper load head at constant rate of 3.6 μm/s. A constant confining pressure of 100 MPa was used for all experiments. Differential stress was estimated as the difference between the axial stress and the confining pressure.

The sample was loaded until the interface failed, resulting in rapid slip occurring on the pre-existing fault. When slip events occur, the sample shortens, resulting in the rapid downward motion of apparatus loading frame relative to the pressure vessel. The optical displacement sensor was mounted on the vessel as shown in Figure 1, and records displacement of the load head relative to the stationary pressure vessel.

To assist in recording and reconstructing the slip-event progression, four different sensors are used.

1. Seismometer: A Marks Products L4C single component seismometer mounted on the apparatus loading frame was used to trigger data acquisition. The seismometer generates a voltage signal proportional to the velocity difference

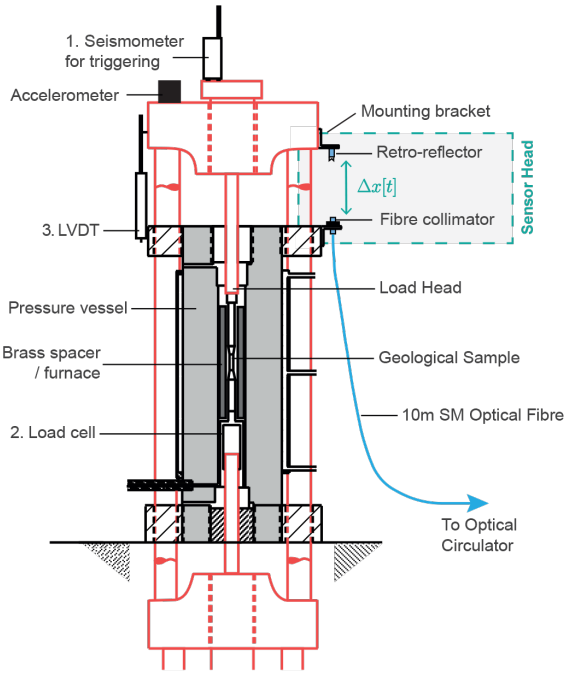

Fig. 1. Schematic cross section of the upper portion of triaxial deformation apparatus. The loading frame is indicated in red. The optical sensor head is mounted at $\Delta x[t]$, indirectly measuring sample displacement.

between the proof-mass and housing. A threshold trigger begins data acquisition upon detection of a slip with velocities ≥ 0.01 m/s.

2. Load Cell: Strain gauges mounted in a full Wheatstone bridge configuration on an internal load cell are used to record the axial load before and after the slip-event. Data is sampled at 100 S/s and recorded at 1 S/s.

3. LVDT: A Linear Variable Displacement Transducer (LVDT) provides an absolute measurement of displacement during slip with a resolution of 600 nm. Data from the LVDT is recorded at a rate of 1 S/s. Measurements are calibrated to adjust for elastic strain that is stored in the apparatus frame during loading, then released during slip [9].

4. Optical system: Operates at 1 MS/s. Described in detail in the following section, the optical system uses remote sensing of the load head position to record the higher frequency characteristics of the slip event evolution. Mounted in the same position on the apparatus as the LVDT, the absolute readout of the optical system is calibrated by the LVDT readout during post-processing. This system achieves a 30 pm/$\sqrt{\text{Hz}}$ at 10 kHz resolution, as shall be demonstrated in the later sections.

B. Optical System

The optical system developed to capture displacement during small seismic events is based on a Mach-Zehnder heterodyne interferometer (Fig. 2). Light from a 1550 nm fiber laser is separated into two paths using an optical fiber coupler with a splitting ratio of 50% (referred to as a 50/50 beam splitter in Fig. 2). Light in the upper path is frequency shifted using a fiber-coupled acousto-optic modulator (AOM) and serves as an interrogating signal field. The lower path serves as a reference local oscillator. A optical circulator is used to separate the return beam. The optical fiber collimator is used to couple light into free-space. A retro-reflecting corner cube is used to reflect light back towards the fiber collimator where it is coupled back into the optical fiber. All the light entering the fiber collimator is separated using the optical circulator, into a second 50% splitting ratio fiber coupler where it is interfered with the local oscillator.

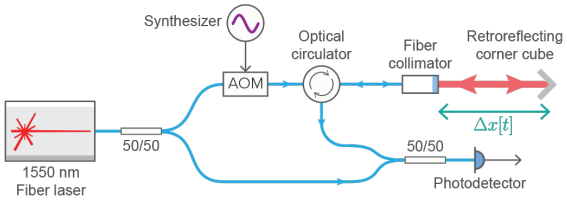

Fig. 2. Schematic overview of the Mach-Zehnder heterodyne interferometer used to measure displacement. Not shown is a long fiber that separates the 'Optical circulator' and 'Fibre collimator' that enables the sensor head to be positioned remotely from the optical setup.

The electric field exiting the laser can be described mathematically by the equation

$$\mathbf{E_0}(\mathbf{t}) = E_0 e^{i\omega_0 t} \tag{1}$$

where E_0 and $\omega_0 = 2\pi f_0$ represent the electric field amplitude and angular frequency of the laser respectively. The signal and local oscillator electric fields exiting the first optical fiber splitter are

$$\mathbf{E_s}(\mathbf{t}) = r_1 E_0 e^{i\omega_0 t} \tag{2}$$

and

$$\mathbf{E_{LO}}(\mathbf{t}) = i t_1 E_0 e^{i\omega_0 t} \tag{3}$$

where r_1 and t_1 represent generic amplitude splitting ratios of the first optical fiber coupler. For an equal 50 % power splitting ratio $R = T = \frac{1}{2}$, the amplitude splitting ratio is $r = t = \frac{1}{\sqrt{R}} = \frac{1}{\sqrt{2}}$. The factor of $i = e^{i\pi/2}$ included in the electric field definition for $\mathbf{E_{LO}}(\mathbf{t})$ is necessary to conserve energy and applies to the transmit port of the fiber coupler as per convention.

The frequency of the light passing through the acousto-optic modulator is shifted by a carrier frequency (ω_h), producing an electric field described by

$$\mathbf{E_h}(\mathbf{t}) = r_1 E_0 e^{i(\omega_0+\omega_h)t} \tag{4}$$

The frequency shifted light exiting the acousto-optic modulator passes through the optical circulator before propagating into free-space through an optical fiber collimator. It is important to note that this system's implementation in optical fiber enables the fiber collimator to be positioned a long distance from the rest of the optical system.

Light exiting the fiber collimator travels some distance, $\Delta x[t]$, to a retro-reflecting corner cube attached to the compression apparatus. The large diameter of the retro-reflecting corner cube and spot size of the fiber collimator allows for a small range ($\sim 2mm$) of off axis motion between it and the fiber collimator without signal strength loss. This is advantageous as a horizontal shift can occur both during the strain buildup period prior to a slip and in the mechanical shaking after the slip event.

Light reflected back towards the fibre collimator is coupled into an optical fiber having travelled a round-trip distance of $2\Delta x[t]$. This round-trip propagation appears as a phase shift in the received electric field. This phase shift is proportional to the total distance divided by the wavelength of the laser, λ;

$$\mathbf{E_r}(\mathbf{t}) = r_1 E_0 e^{i\left((\omega_0+\omega_h)t + 2\pi\left(\frac{2\Delta x[t]}{\lambda}\right)\right)} \tag{5}$$

The light captured by the fiber collimator (which in this analysis is assumed to be lossless) is directed to a second fiber splitter, via the optical circulator, to be recombined with the reference local oscillator.

Polarization is aligned using fiber polarization controllers before being interfered at a high-bandwidth photodetector, producing a voltage waveform containing information about the *relative* frequency and phase of the interfering electric fields. The signal and local oscillator electric fields, after recombination at the second optical fiber coupler, are

$$\mathbf{E_r}(\mathbf{t}) = r_1 r_2 E_0 e^{i\left((\omega_0+\omega_h)t + 2\pi\left(\frac{2\Delta x[t]}{\lambda}\right)\right)} \tag{6}$$

and

$$\mathbf{E_{LO}}(\mathbf{t}) = i^2 t_1 t_2 E_0 e^{i\omega_0 t} \tag{7}$$

where r_2 and t_2 represent the electric field splitting ratios of the second optical fiber coupler. The second output port of the coupler has been ignored in this analysis.

When $\mathbf{E_r(t)}$ and $\mathbf{E_{LO}(t)}$ interfere at the photodetector, producing a field ($E_{PD}(t)$) with power equal to

$$\mathbf{P_{PD}(t)} = E_{PD}(t) \cdot E^*_{PD}(t) \tag{8}$$

where

$$E_{PD}(t) = \mathbf{E_r(t)} + \mathbf{E_{LO}(t)} \tag{9}$$

$E^*_{PD}(t)$ denoting the complex conjugate of the electric field at the photodetector. The voltage signal produced by the photodetector's transimpedance amplifier from this field power is then

$$\mathbf{V_{PD}(t)} \propto \mathbf{P_{PD}(t)} = A\cos\left(\omega_h t + 4\pi\frac{\Delta x[t]}{\lambda}\right) \tag{10}$$

where A represents the voltage amplitude. Figure 3 presents a summary of the phase propagation through the optical system for reference.

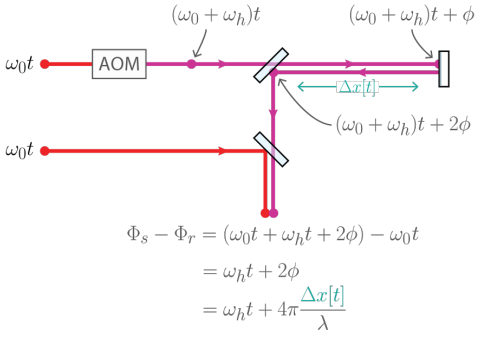

Fig. 3. Summary of the phase progression of the electric fields through the Mach-Zehnder interferometer. Path length changes between the signal arm (top) and local oscillator (bottom) appear in the phase of the heterodyne beat-note produced by the interference of the two electric fields at the photodetector.

C. Digital Acquisition and Calibration

The voltage waveform produced by the photodetector is digitized at 240 MS/s using a National Instruments NI-5761 analog-to-digital converter (ADC) interfaced with a PXI-7954 FlexRIO FPGA. The 240 MS/s signal is down-sampled to the operational clock frequency of a digital phase-locked loop (PLL), 80 Ms/s, using a digital second-order cascaded integrator-comb filter.

The digitally implemented phase-locked loop is used to track the phase of the digitized and down-sampled beat-note in the photodiode voltage signal (as in Equation 10) [10]. The functional architecture of the PLL used in this experiment is shown in Figure 4.

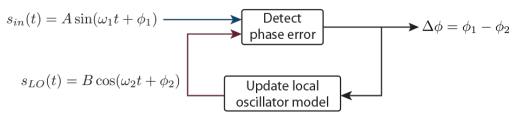

Fig. 4. Functional architecture of a phase-locked loop.

Phase-locked loops measure phase by continuously tracking the phase difference between the input signal and a reference local oscillator. Consider the input signal $s_{in}(t)$ and local oscillator $s_{LO}(t)$ with amplitudes A and B, angular frequencies ω_1 and ω_2, and phases ϕ_1 and ϕ_2:

$$s_{in}(t) = A\sin(\omega_1 t + \phi_1) \tag{11}$$
$$s_{LO}(t) = B\cos(\omega_2 t + \phi_2) \tag{12}$$

The PLL detects the instantaneous phase difference $\Delta\phi = \phi_1 - \phi_2$ by multiplying the input signal and local oscillator signals:

$$s_M(t) = \frac{AB}{2}[\sin(\omega_1 - \omega_2)t + \Delta\phi) + \sin((\omega_1 + \omega_2)t + \phi_1 + \phi_2)] \tag{13}$$

The higher frequency component is attenuated using a low-pass filter. When $\omega_1 = \omega_2$, the low-pass filtered signal becomes:

$$s_F(t) = \frac{AB}{2}\sin(\Delta\phi) \tag{14}$$

If $\Delta\phi \ll 1$, then equation 14 can be approximated to be $s_F(t) \approx \frac{AB}{2}\Delta\phi$ using the small angle approximation for sine. The phase difference $\Delta\phi$ forms an error signal used to generate feedback control to update the phase of the local oscillator. The phase-locked loop's controller generates feedback to continuously drive this error signal to zero, meaning the small angle approximation remains valid. The record of all changes made to the phase of the local oscillator provides a measurement of the input signal's phase with respect to that of the local oscillator over time.

The phase-locked loop used in this study produces simultaneous measurements of the input signal's frequency, phase, and amplitude. Displacement information of slip events is contained in the phase of the beat-note produced by the heterodyne interferometer. Phase data in units of cycles is converted into displacement by multiplying it by the laser wavelength, λ. In this system, λ = 1.552 μm, which means a 1,000 cycle excursion in phase corresponds to a displacement of approximately 1.55 mm. Phase is tracked in a continuous manner, which enables sub-wavelength measurements over multiple wavelengths of dynamic range.

Data produced by the LVDT and load cell sensors, described in section A, were recorded using 1 S/s ADCs.

Displacement information produced by the phase-locked loop is calibrated against the absolute displacement measurement provided by the LVDT. This calibration reduces the effects of uncertainty in the absolute optical wavelength of the laser at the time of measurement. As shown in Figure 5, the absolute displacement measurement from the LVDT gives the range between the initial and final values recorded within the two second window. The first second of data prior to the slip event is used as reference for the operational noise floor of the sensor.

3. RESULTS

The operation of the optical displacement sensor was tested using three Fontainebleau sandstone samples, producing 13 episodic rapid-slip events. Sample behavior during experiments is characterized by an initial period of elastic loading, followed by a poorly defined yield point and the onset of permanent deformation. The majority of deformation localizes as slip and fracture damage on the pre-ground fault surface. After varying displacements, sliding behaviour transitions from slip-hardening

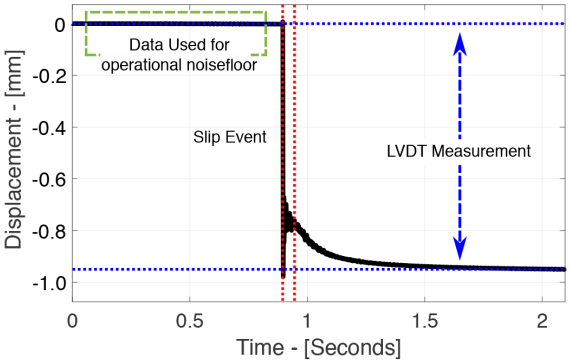

Fig. 5. An example of displacement measured in the 2 second window as taken from a 950 μm slip-event. Absolute displacement over the slip events are calibrated using the absolute LVDT measurements. Displacement data prior to the slip is used in calculating operational noise.

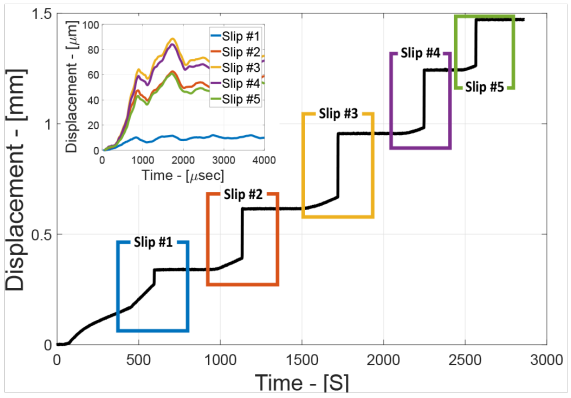

Fig. 6. Displacement as measured by the LVDT for deformation of a single sample showing multiple slip-stick events over a the length of the experiment. Insert: Each stick-slip event is isolated and measured by the optical displacement sensor, revealing micro-variations in the slip displacement profile.

creep to stick-slip, manifest by periods of elastic loading interspersed with large stress drops and frictional sliding along the fault surfaces. The geological significance of this type of experiment is discussed elsewhere (e.g. Hayward et al. 2016 [7]).

The size of the slip events is driven by the sudden release of elastic strain energy stored in the sample, assembly and loading frame (Shown in red in Figure 1). The rapid release of the elastic energy causes the apparatus to resonate as elastic waves associated with rupture and slip propagate and reflect within the steel frame. This mechanical response has not been separated in the presented results as isolating and removing these effects is the subject of ongoing research.

A. Time domain measurement

Figure 6 shows time series data of a typical displacement event with a single sample using both the LVDT and interferometric displacement sensor. The black trace, in the main figure, is of data captured by the LVDT and shows five slip events (highlighted by coloured boxes for clarity) recorded over a single run recorded at 1 S/s. A measurement range of approximately 1.5 mm was required to record the total shift of the load head while testing a single sample.

High-resolution displacement measurements of each slip event produced by the interferometric displacement sensor are shown in the inset of Figure 6. The optical readout yields a higher resolution displacement profile compared to the LVDT readout and with a higher sample rate. Due to limitations in the availability of high access speed memory, only the 2 second window centered on each slip event is saved to long-term memory. The recording system using the loading time between slip events to perform the slower operations of shifting data between the two memory systems.

The profiles within the time series arise from a combination of material properties and the mechanical response of the triaxial compression apparatus. This sample yielded five slip events, with displacements ranging from 10 μm (blue) to 92 μm (yellow).

Across the three samples tested, slip displacements ranged between 10 μm and 225.7 μm.

B. Velocity Limits

By using a PLL the optical displacement sensor is able to operate over a large dynamic range with high precision. The ability of the PLL to follow high velocities (e.g. instantaneous displacement over small time series) is set by the bandwidth of the PLL feedback loop, and hence limits the maximum velocity that can be recorded. The maximum instantaneous phase change of the carrier between two consecutive data points must not exceed $\pm\pi/2$, or cycle slip within the PLL will occur. This generates an operational range for the phase difference between timestamps of the PLL of:

$$-\frac{\pi}{2} \leq \left(\Phi[t+\frac{1}{f_{PLL}}] - \Phi[t]\right) \leq \frac{\pi}{2} \tag{15}$$

Cycle slip can cause any large displacement occurring between time-stamps to be falsely recorded as a smaller displacement change by the PLL.

To define a maximum velocity (V_{limit}), we refer to Equation 10, where velocity acts as a modulation of the carrier frequency. The combined phase progression of the local oscillator and equivalent phase progression added by the velocity must be within the operational range for the PLL, defined in Equation 15:

$$-\frac{\pi}{2} \leq \left(2\pi\frac{f_{LO}}{f_{PLL}} + \frac{4\pi}{\lambda}V\frac{1}{f_{PLL}}\right) \leq \frac{\pi}{2} \tag{16}$$

Such that V is the average velocity of the displacement between time-stamps. The maximal velocity before displacement is underestimated (V_{limit}), also known as the the 'confusion limit', occurs when:

$$V_{limit} = \pm\frac{\lambda}{8}f_{PLL} - \frac{\lambda}{2}f_{LO} \tag{17}$$

where f_{PLL} is the clock frequency operating the phase lock loop. Using a 1550 nm wavelength laser, a 80MHz clock frequency and a 26.4 MHz carrier frequency, the lowest confusion limit is equal to a velocity of 4.96 m/s. Across all 13 recorded slip events maximum recorded instantaneous velocities ranged between 0.0416 m/s and 0.2570 m/s, implying a stability in the phase measurement during deformation experiments.

C. Frequency domain measurement

Figure 7 presents the amplitude spectral density envelope of the displacement profiles of all 13 recorded slip-stick events within their 2 second window. This spectrum shows the sensitivity of the displacement sensor reaches 30 pm/$\sqrt{\text{Hz}}$ at 10 kHz allowing for fine observations of slip-stick displacements.

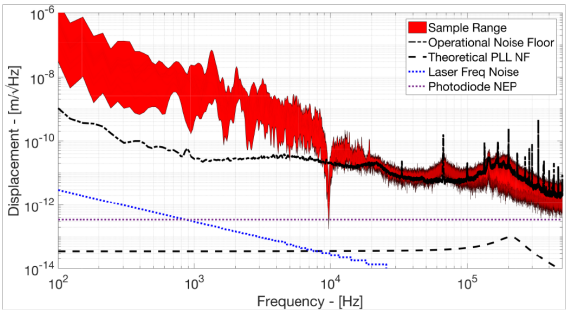

Fig. 7. Amplitude spectral density of the slip displacement compared to theoretical and measured sensor limits. The recorded slip events of interest are above the noise levels at frequencies below 10 kHz within the slip-event window.

The operational noise floor, as shown in Figure 7, this is obtained as an average spectra of noise witnessed in the periods prior to each slip-event (as indicated in Figure 5). The operational noise floor had minimal variance between slip events. The limiting factors of the operational noise floor have not been fully determined. However it is expected that technical sources such as the mechanical disturbance of the long optical fibre to the collimator and the general vibrations of the triaxial machine during loading are likely culprits. The frequency profile of the operational noise floor was noted to shift during the operation of the deformation apparatus, compared to the system at rest.

The theoretical Phase Lock Loop Noise Floor (Theoretical PLL NF in Figure 7) was derived using the methodology described in Roberts 2016 [10]. The PID (proportional–integral–derivative) controller for the PLL was tuned to have a unity gain frequency of 200 kHz to ensure system stability during the slip events. This resulted in gain peaking at the unity gain frequency in the theoretical PLL and the operational noise floor. Information above this unity gain frequency was recoverable through the undoing of the PID closed-loop frequency response.

The system operates using a free running fibre laser, and has a 10 m long optical fiber to deliver the light to the collimator on the apparatus. The local oscillator path is about a meter long, so the laser frequency noise contribution into the length measurement will become limit. The theoretical laser frequency noise coupling into the displacement measurement is give by Hrabina et al. 2013 [11]:

$$\Delta x_{freq} = \Delta L(1 - \frac{c}{c + \lambda n \Delta f}) \tag{18}$$

in which n is the refractive index of the optical fibre, here 1.425, and Δf is the frequency noise of the laser as given by the manufacturer. ΔL is the effective path length difference between the signal path and the local oscillator pathway before the photodetector. The laser is an Orbits Lightwave, Ethernal Slowlight Laser Module, model ETH-10-1550.12-2-PZ10, which has a quoted frequency noise of 1 Hz/$\sqrt{\text{Hz}}$ at 100 kHz with a $1/f$ slope.

The photodiode Noise Equivalent Power (NEP) is taken from the specifications of the New Focus, Model 1811 125-MHz, Low Noise Photo Receiver. This is done by applying Equation 19 such that; the NEP of the photodiode at the carrier frequency is p_{NEP} ($19.9pW/sqrt\text{Hz}$ at 26.4 MHz), the photodiode response at 1550 nm wavelength is H_λ ($1\ A/W$), the trans-impedance gain is R (40 kΩ), the gain applied by amplitude of the carrier signal is A (1.8 V/V) and the gradient of volts to displacement around the zero point of the PLL is $G_{\delta x}$ ($1.55\mu m/4V$).

$$NEP = \frac{p_{NEP} H_\lambda R G_{\delta x}}{A} \tag{19}$$

$$NEP = \frac{(19.9pW/\sqrt{\text{Hz}})(1A/W)(40k\Omega)(1.55\mu m/4V)}{(1.8V/V)} \tag{20}$$

The resulting photodiode detection limit is 0.171 pm/$\sqrt{Hz}$. In the constructed sensor the shot noise is lower than the NEP, at 0.018 pm/$\sqrt{Hz}$.

The optical displacement sensor is able to record slip-event displacements down to $10^{-10}\ m/\sqrt{\text{Hz}}$ up to 100 kHz, limited by the current photo detector implementation. Also of note is that during the measurement, the sensor records any mechanical vibrations of the triaxial compression apparatus. Some suppression of the displacement is expected due to the mass of the triaxial compression apparatus. Elimination of the mechanical response is an area of ongoing development.

4. EXPANSION TO MULTI-CHANNEL

As an expansion of the initial implementation of the optical displacement sensor, additional sensor heads can be added to the system in a parallel signal path. This is enabled by the placement of the AOM in the signal path rather than the local oscillator path. The additional sensing path joined to the system by changing the initial and final 50:50 fiber coupler into 3-to-1 fiber coupler. An additional AOM (at a different carrier frequency), optical circulator and fiber collimator are required. In principle this can be repeated multiple times, however carrier frequency spacing needs to be chosen carefully to eliminate cross-coupling, and is also set by the PLL update rate.

Optical power levels onto the single photodiode need to be adjusted so that it does not saturate the photodiode output into the ADC. Inside the digital acquisition and calibration system, multiple PLL operate in parallel at their respective carrier frequencies. All paths can be calibrated using the same LVDT data, as the net displacement of both locations over the slip event should be equal to the slip distance.

Future work is underway to install multiple sensor heads to record the mechanical resonance of the triaxial compression apparatus with the aim of isolating sample displacement from the apparatus response during slip events.

5. CONCLUSION AND FURTHER WORKS

Using our new optical displacement sensor we have been able to measure seismic slip events with sub-nanometer resolution over a dynamic range of several millimeters, with a maximum velocity of 0.2570 m/s. It is projected the measurement method used has a greater capacity than this, with a dynamic range of multiple centimeters and a velocity limit of 12.4 m/s for the given implementation.

The module was developed to enhance investigation of processes occurring during laboratory-scale earthquakes [7] and

provides a significant advance in the temporal resolution of displacement and velocity data acquisition during laboratory slip experiments. No major alteration to the triaxial apparatus was required to implement the system. Through usage of a remote optical head, the optical displacement sensor is immune to electromagnetic interference at the operation point. The controller of the phase-lock loop implemented operates with a unity gain frequency of 200 kHz, resulting in an equivalent unity gain recovery of displacement. The system can also be operated remotely fulfilling the need for isolation of the high pressure vessel during use. As such the system meets the design criteria set out for the system.

Efforts are ongoing to further decrease the observed noise floor of the system and to characterise and isolate the mechanical vibrations of the triaxial apparatus.

6. ACKNOWLEDGEMENT AND FUNDING

This research was supported by the Australian Research Council, under the ARC Centre of Excellence for Gravitational Wave Discovery, Grant No. CE170100004, and ARC Future Fellowship FT130100329. Stephen Cox and Kathryn Hayward were supported by Australian Research Council Discovery, Grant No. DP130102687. Kathryn Hayward acknowledges scholarship support of the Australian Government Research Training Program. Equipment development was funded by an Australian National University Major Equipment grant allocated in 2016.

7. DISCLOSURES

The authors declare no conflicts of interest.

REFERENCES

1. R. H. Sibson, "Fault zone models, heat flow, and the depth distribution of earthquakes in the continental crust of the United States," Bulletin of the Seismological Society of America **72**, 151–163 (1982).
2. C. H. Scholz, *The Mechanics of Earthquakes and Faulting* (Cambridge University Press, 2019), 3rd ed.
3. G. Di Toro, A. Niemeijer, A. Tripoli, S. Nielsen, F. Di Felice, P. Scarlato, G. Spada, R. Alessandroni, G. Romeo, G. Di Stefano *et al.*, "From field geology to earthquake simulation: a new state-of-the-art tool to investigate rock friction during the seismic cycle (shiva)," Rendiconti Lincei **21**, 95–114 (2010).
4. T. Shimamoto, "A new rotary-shear high-speed frictional testing machine: its basic design and scope of research." Jour. Tectonic Res. Group of Japan **39**, 65–78 (1994).
5. J. G. Spray, "Artificial generation of pseudotachylyte using friction welding apparatus: simulation of melting on a fault plane," Journal of Structural Geology **9**, 49–60 (1987).
6. M. Paterson, "A high-pressure, high-temperature apparatus for rock deformation," International Journal of Rock Mechanics and Mining Sciences & Geomechanics Abstracts **7**, 517 – 526 (1970).
7. K. S. Hayward, S. F. Cox, J. D. Fitz Gerald, B. J. J. Slagmolen, D. A. Shaddock, P. W. F. Forsyth, M. L. Salmon, and R. P. Hawkins, "Mechanical amorphization, flash heating, and frictional melting: Dramatic changes to fault surfaces during the first millisecond of earthquake slip," Geology **44**, 1043–1046 (2016).
8. D. A. Lockner, B. D. Kilgore, N. M. Beeler, and D. E. Moore, *The Transition From Frictional Sliding to Shear Melting in Laboratory Stick-Slip Experiments* (American Geophysical Union (AGU), 2017), chap. 6, pp. 103–131.
9. K. S. Hayward and S. F. Cox, "Melt welding and its role in fault reactivation and localization of fracture damage in seismically active faults," Journal of Geophysical Research: Solid Earth **122**, 9689–9713 (2017).
10. L. E. Roberts, "Internally sensed optical phased arrays," Ph.D. thesis, Research School of Physics and Engineering, The Australian National University (2016).
11. J. Hrabina, J. Lazar, M. Holá, and O. Cíp, "Frequency noise properties of lasers for interferometry in nanometrology," Sensors (Basel, Switzerland) **13**, 2206–2219 (2013).